Spatially configuring wrinkle pattern and multiscale surface evolution with structural confinement

Spatially configuring wrinkle pattern and multi-scale surface evolution with structural confinement

By *Ding Wang,[1] Nontawit Cheewaruangroj,[2] Yifan Li,[1] Glen McHale,[1] Yinzhu Jiang,[3] David Wood,[4] John Simeon Biggins,[2]* Ben Bin Xu[1]**

[1] Mr. Ding Wang, Dr. Yifan Li, Prof. Glen McHale, Dr. Ben B. Xu,
Smart Materials and Surfaces Laboratory,
Faculty of Engineering and Environment,
Northumbria University,
Newcastle upon Tyne, NE1 8ST, UK
*E-mail: ben.xu@northumbria.ac.uk

[2] Mr. Nontawit Cheewaruangroj, Dr. John S. Biggins,
Cavendish Laboratory,
19 JJ Thomson Avenue,
Cambridge University,
Cambridge, CB3 0HE, UK
**E-mail: jsb56@cam.ac.uk

[3] Dr. Yinzhu Jiang,
State Key Laboratory of Silicon Materials,
Laboratory of Advanced Materials and Applications for Batteries of Zhejiang Province,
School of Materials Science and Engineering,
Zhejiang University,
Hangzhou, Zhejiang, 310027, P. R. China

[4] Prof. David Wood,
Department of Engineering,
Durham University,
Durham, DH1 3LE, UK

Keywords: Elastic instabilities, Wrinkling, Micro-pattern, Bravais lattice, Morphological bifurcation.

Abstract:

Surface elastic instabilities, such as wrinkling and creasing, could enable a convenient strategy to impart reversible patterned topography to a surface. Here we focus on the classic system of a stiff layer on a soft substrate, which famously produces parallel harmonic wrinkles at modest uniaxial compression that period-double repeatedly at higher compressions and ultimately evolve into deep folds and creases. By introducing micron-scale planar Bravais lattice holes to spatially pattern the substrate, we can guide these instabilities into a wide variety of different patterns, including wrinkling in parallel bands and star shape bands, and radically reduce the threshold compression. We are able to understand our experimental patterns and thresholds by considering a simple plane-strain model for the patterned substrate-deformation, decorated by wrinkling on the stiff surface layer. Our experiments also show localized wrinkle-crease transitions at modest compression, yielding a hierarchical surface with different generations of instability mixed together. By varying the geometrical inputs, we demonstrate control over the stepwise evolution of surface morphologies. These results demonstrate considerable control over both the patterns and threshold of the surface elastic instabilities, and have relevance to many emerging applications of morphing surfaces, including in wearable/flexible electronics, bio-medical systems and optical devices.

INTRODUCTION

Elastic instabilities such as wrinkles, creases and folds, are usually considered as unwanted when they appear in engineering structures, as they can precipitate fracture and failure. Recently, scientists have significantly advanced our understanding of the mechanics of elastic instabilities [1-7], opening the possibility of transforming these unwanted phenomena into tools for producing useful shape changes in response to a range of external stimuli.[8-13] The latter perspective has enabled engineering opportunities with self-adaptive/autonomous structures in low dimensions and has implications in many different contexts such as micro-/nano-fluidics,[14-16] flexible electronics,[17,18] adhesion,[19,20] organic solar cells,[21] tunable optics,[22-24] wettability,[25-27] and promising methods for surface patterning[1,28-31]. While our scientific/technical understanding has advanced, there remains much to be explored about the control of instability morphology, and in particular how to configure instabilities, such as wrinkling and creasing, to desired patterns with selective distribution covering the surface and bespoke thresholds for the formation and evolution of instabilities.

When compressing a bilayer elastomer system with a stiff skin layer, the formation of surface wrinkles releases in-plane compression of the stiff layer, as bending is energetically more favourable than compression. With further compression, the wrinkles experience further bifurcations, including period-doubling and quadrupling,[5,32] and finally develop into deep folds/creases.[33-35] These wrinkling and post-winkling behaviours have been well understood by considering the intrinsic material properties of a bilayer (module mismatch, Poisson's ratio, etc), structural variables (thickness) and the pre-strains imposed on the system. However, thus far, such compressive instabilities have been studied in non-patterned surface systems, where both wrinkling and further bifurcations occur as global events, spanning the entire surface at once. Notably, Huck and co-workers investigated the spontaneous formation of patterns of aligned buckles on a flat gold/PDMS bilayer with placed confinement.[36] Kim and co-workers studied the morphological transitions on the surface of a bilayer under a biaxial compressive stress and revealed a mechanism to

controllably generate a 2D wrinkle/fold pattern on the entire film surface.[3] Wang and Zhao have summarised the instability bifurcations on flat surfaces and generated a phase diagram by considering the geometrical variations and module mismatches.[37,38] Recent work has also studied bilayer instabilities on surfaces with curvature,[39-42] where wrinkling is still a global event, but where the pattern and threshold are influenced by the curvature. Here we investigate whether we can induce wrinkling and further bifurcations in patterned sub-regions of a bilayer by explicitly patterning the surface, thus paving the way for bespoke instability morphologies at bespoke thresholds.

Such Controllable formation and development of instabilities in targeted regions are highly desirable for engineering applications such as strain sensing structures, actuating units in wearable devices, healthcare devices, bio-fluidic devices, etc. In this paper, we demonstrate a simple strategy to generate 2D harmonic surface wrinkle patterns and control transitions thresholds on the surface of an elastic bilayer under uniaxial compressive stress, by employing structural confinement (a Bravais lattice of holes) to regulate the in-plane stress map on a surface. The regions adjoining the Bravais lattice holes nucleate harmonic wrinkle networks at small compressive strains due to confinement. At higher compression, the wrinkle-crease transition is initialized at selected areas with strain energy localization guided by the curved geometrical boundary from the edge of Bravais lattice holes, which then finally develop into a global creasing. The dynamics of the formation of planar wrinkle patterns and localised wrinkle-crease transition are studied, and we illustrate a distinct stepwise instability pattern evolution towards a hierarchical surface. We also combine experiments with numerical simulations to track the in-plane stress state and study the generation of harmonic morphology under the confinement.

RESULTS AND DISCUSSION

The Bravais lattice template was prepared by lithographically fabricating SU-8 pillars on a silicon wafer (**Figure 1a**). The Bravais pattern was then transferred to a soft substrate by coating the template with a thin (125 μm) layer of softer PDMS (shear modulus ~ 0.1 MPa),

which was then cured on a substantially pre-stretched elastic 'mounting' base layer (thickness ~ 3 mm, shear modulus ~ 0.35 MPa). After curing, the PDMS structure was released from the template, aided by a salinization treatment applied to the template to reduce surface adhesion. Under compression, patterned surfaces composed of polygonal shapes, *i.e.* triangles, squares, etc, can yield strain energy concentrations and localised bulk deformations around their corners, making it difficult to reach the energy threshold to trigger the surface instability. Therefore, we used patterned surfaces with circular (hole) shapes to avoid strain energy localization and also expected that the curvatures can be used to regulate the formation of instabilities. Two different Bravais lattices (**Figure 1b–1e**), square and centered square, were employed with varied geometrical aspect ratios, hole diameter (Φ), hole distance (D), hole depth (h), to establish a range of patterned soft surfaces. Finally, oxygen plasma treatment was used to create a thin stiff layer on the patterned soft substrate (**Figure 1f**) prior to the compression.

Upon subsequent release of the mounting layer from a pre-stretched length L_0 to a length L, the patterned PDMS layer is under compression, which we characterize by the nominal (far-field) uniaxial compressive strain $\varepsilon = L_0/L - 1$. The oxygen plasma effect was examined on a surface with pattern features of D =160 μm, Φ = 80 μm, h =20 μm. For surfaces without plasma treatment, the holes slowly closed as the compressive strain increased, but no surface wrinkling was observed (**Movie S1**). In contrast, on the plasma treated surface (**Movie S2)**, we observed a series of patterned surface instabilities as compression increased, starting with wrinkles formed at $\varepsilon \sim 0.04$, then in-plane wrinkling bifurcation (period doubling) at $\varepsilon \sim 0.08$, followed by the nucleation of creasing (wrinkling-creasing transition) at $\varepsilon \sim 0.1$, and global creasing at $\varepsilon \sim 0.3$, and finally the closure of lattice holes at $\varepsilon \sim 0.55$.

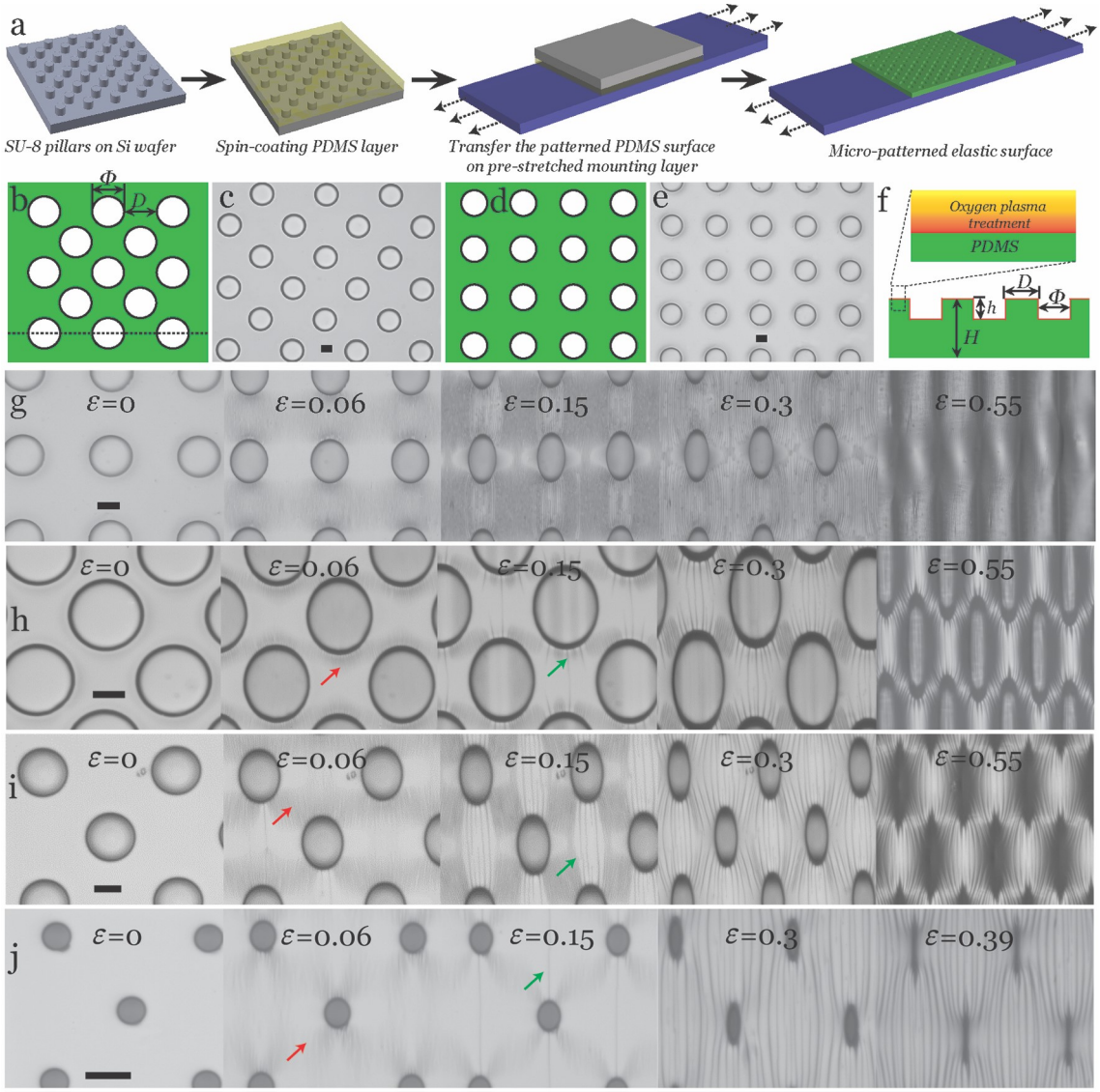

Figure 1. Illustration of design and fabrication process of structural confinements and guided formation of surface morphologies under compression. (a) The structural surface was fabricated by spin-coating a thin PDMS precursor layer on a lithographically made template (SU-8 pillars array on a silicon wafer), then transferring and curing the thin PDMS layer (~ 125 μm) onto the top of a pre-stretched mounting elastomer layer with thickness ~ 3 mm. Two in-plane arrays with varied aspect ratios are designed, (b) illustration and (c) optical microscopy for centered square lattice array, (d) illustration and (e) optical microscopy for square lattice array. (f) The microfabricated surface was treated with oxygen plasma to achieve a stiff skin layer (~ 50 nm). (g) The observation of surface morphology changes on square lattice array patterned surface at different compression levels. (h-j) The observation of surface morphology changes on a centered lattice array patterned surface at the same compression sequences in (g) with different aspect ratios. The wrinkle patterns are marked with red arrows and creases are marked with green arrows. All images in this figure have been formatted with the same scale bar of 20 μm.

The morphological development of the surfaces was characterized under reflected light optical microscopy to study the dynamic surface evolution with different lattice arrays. A series of observations were made at the same strain sequence to reveal surface states at the same deformation level. For the pattern with a square lattice (**Figure 1g**), the in-plane wrinkle pattern appears to be lateral straight stripes and doesn't change much with different aspect ratios (**Figure S1**). For the pattern with centered square lattice, the case is more interesting and we see three types of in-plane wrinkling patterns formed at small compressive stress with a high sensitivity to the aspect ratios of lattice we applied. For D/Φ = 1, an in-plane curved stripes pattern is developed with a strong dependency on the local curvature determined by the lattice hole and aspect ratio of lattice array (**Figure 1h**). Straight wrinkle stripes pattern is evident when D/Φ = 2 (**Figure 1i**), which is similar to the surface patterned with square lattice. However, an in-plane 'star' wrinkle pattern is generated for D/Φ = 4 (**Figure 1j**), the wrinkle morphology shows a 2D periodic distribution around each hole with a 'star' shape, implying a diagonal strain energy localization.

At higher compression, all patterned surfaces develop morphological evolutions showing a wrinkle-crease transition, the surface creases nucleate at the edge of lattice hole perpendicular to the compression direction at $\varepsilon \sim$ 0.06 - 0.013. The creases progress as the compression increases, and fully cover the surface at $\varepsilon \sim$ 0.3. Among these morphological transitions, an interesting phenomenon is discovered that a single crease can be generated on the surface with centered square lattice holes (D = 80 μm, Φ = 20 μm, h = 20 μm). This has great potential to enable new types of surface actuator with targeted compression effects within the scale of a few micrometres. It should also be noted that the critical strains for initializing the transition ($\varepsilon \sim$ 0.06 - 0.013) are much lower than the typical critical strain value of $\varepsilon_{crease} \sim$ 0.35 - 0.55.[2,7] The reason is that the nominal strain level we used as a control parameter doesn't well reflect the strain localization on the structural confined surface. The strain energy localization at a curved boundary near a hole edge for a patterned surface could

be several folds of that on a non-patterned surface. We will discuss these features in more detail later in this report.

To understand the instability patterns (**Figure 2a-2c**) and thresholds observed above, we conducted a numerical analysis by calculating the pattern of deformation under the imposed global compressive strain for lattice patterned surfaces (**Figure 2d**). Deformation around a single hole and square/centered square arrays of holes has been previously studied within linear elasticity,[43,44] and generally produce stress concentrations near the holes. To generalize these results to our lattices, we modelled the patterned substrate as a linear-elastic 2D plane-strain system consisting of an infinite incompressible elastic material containing the appropriate infinite lattice of holes. As seen in **Figure 2e**, we consider a square unit cell of the resulting system (centered square patterned surface), and used Mathematica finite elements to solve the plane strain field in response to an imposed compressive strain, ε_{plain}, in the x direction and, as measured in experiments, a sympathetic extension of 0.3 ε_{plain} in the y direction, and with stress free boundary conditions at the edges of the holes.

In **Figure 2f**, we plot the local maximum compressive strain in our solutions, $\varepsilon_{pattern}$, as a fraction of ε_{plain}, for several different aspect ratios of lattice. We see that the compressive strain is strongly localized around the holes. In centered square lattices with smaller holes, there are also clearly star-shaped patterns of increased compression running between the holes. We show the same plots for a simple square lattice in **Figure S2,** showing compression concentration in lateral straight stripes through the holes at all aspect ratios of pattern.

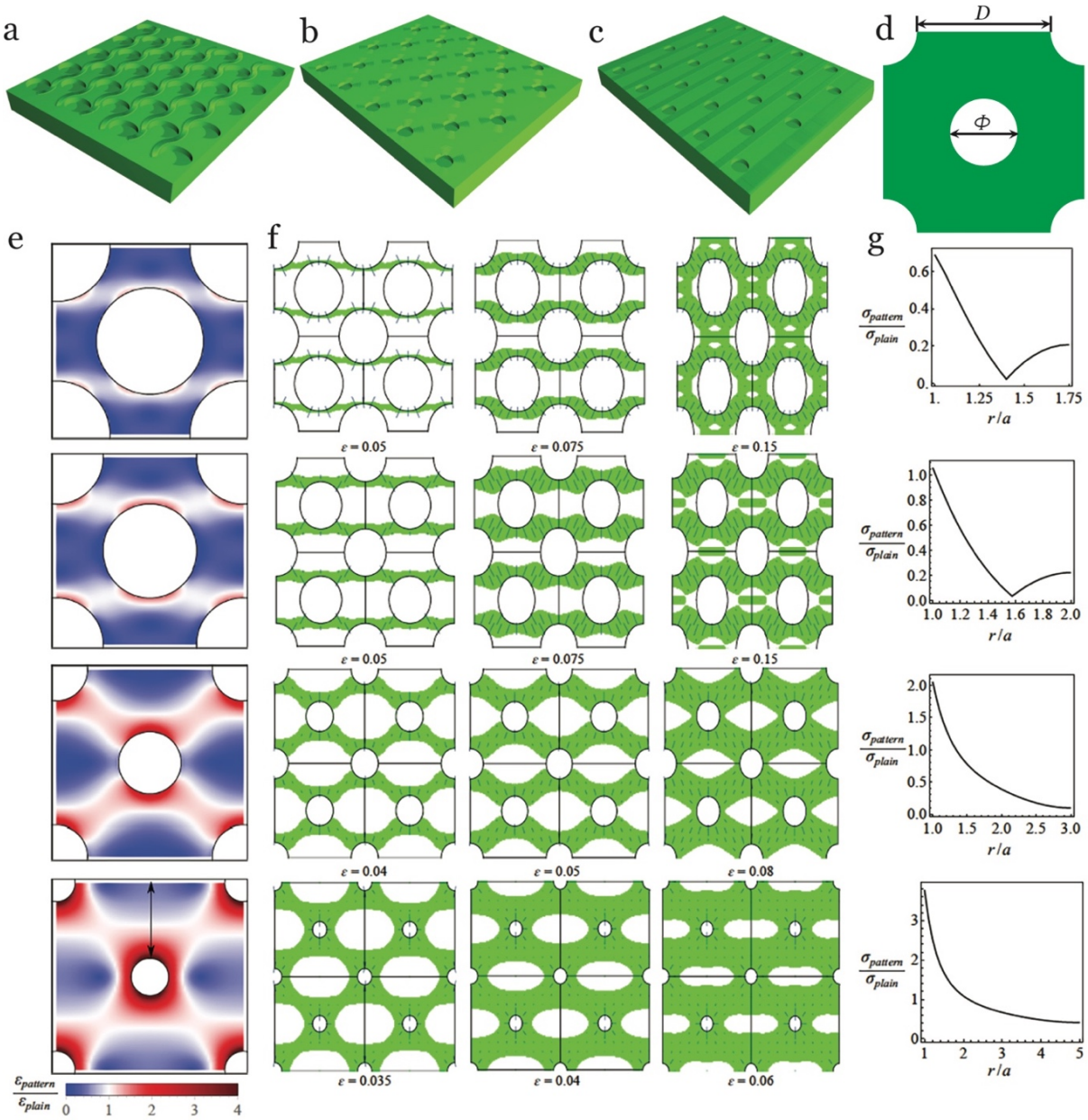

Figure 2. Analytical approach of the generated harmonic winkle patterns.

Three harmonic patterns are generated as (a) curved ribbon, (b) star shape, (c) straight belt. (d) A representative unit area is chosen for numerical analysis. (e) Compression of the patterned substrate relative to the compression of the non-patterned substrate. Blue and red indicate the less and more compressive areas. (f) Evolution of wrinkling region as a function of applied strain in the deformed bilayer system with patterned holes. Green areas are the wrinkling regions. Lines indicate the direction along which the wrinkles will grow while their lengths are the relative distance from the wrinkling threshold. (g) Compressive stress in the stiff layer in the patterned bilayer system relative to the non-patterned system values at different position from the rim of the hole of radius a (maximum stress) to the edge of the unit cell (see arrow in (e) bottom). All plotted with D/Φ = 0.75, 1, 2 and 4.

We next calculate the wrinkling pattern on the stiff plasma-treated skin that decorates this base-state deformation. To do this, we first calculate the compressive stress σ_c in the thin film, assuming it has a Poisson ratio of ν_f=0.3 directly follows the deformation in the soft substrate. The value of this compressive stress, as a fraction of the compressive stress that would be observed in a non-patented system, is plotted for each lattice in **Figure 2g**, as a function of distance from the centre of the central hole, along the line shown in the bottom figure of **Figure 2e**. For a centered square lattice patterned surface, we see that the compressive stress is strongly enhanced at the edge of hole, particularly in lattices with small holes, explaining why wrinkling occurs earlier in patterned systems. To predict wrinkling patterns, we apply the standard result for wrinkling on a substrate, which is that wrinkling will occur if $\sigma_c > \frac{1}{4}\left(3\frac{\bar{E}_s}{\bar{E}_f}\right)^{2/3}\bar{E}_f$, where $\bar{E}_f$ and $\bar{E}_s$ refer to the plane-strain elastic modulus for the oxidized stiff layer and PDMS substrate, respectively, which are related to the Young's moduli, E, by $\bar{E} = E/(1-\nu^2)$, where ν is the Poisson ratio. Taking the physically reasonable modulus ratio $\bar{E}_f/\bar{E}_s$ = 100, we plot, in **Figure 2f**, how the predicted wrinkle regions grow as the global compression is increased. We see, in accordance with experiment, that moving from large holes to small holes does indeed change the wrinkling pattern from wavy lines, to straight lines, to stars, and that the patterns with smaller holes wrinkle at smaller global compressions, because the compressive stress is more concentrated around the hole.

After plasma treatment for 10 seconds, the surface modulus measurement (**Figure S3**) obtained by AFM indentation suggests the plane-strain elastic modulus mismatch between the film and the substrate is about $\bar{E}_f/\bar{E}_s \sim 25$. Accordingly, the critical strain for wrinkling from linear stability analysis [45-48] is $\varepsilon_W = 0.25(3\bar{E}_s/\bar{E}_f)^{2/3} = 0.061$, which agrees well with our result of $\varepsilon \sim 0.068 \pm 0.008$ for a non-patterned surface (**Figure S4**). However, it doesn't agree with the case of a lattice patterned surface, in which wrinkle patterns are already present at $\varepsilon = 0.06$, indicating that wrinkling occurs at a lower threshold strain as a result of strain energy localization near the lattice holes. Furthermore, according to the report from Kim and co-workers, as compression is increased in systems with $\bar{E}_f/\bar{E}_s \sim 25$, wrinkles

are expected to period double then evolve into creases. We expect patterning to also reduce the thresholds for these further bifurcations, but they cannot be effectively identified under reflective optical microscopy.

To unveil more details, we used AFM to track the surface morphology changes as the compressive strain was gradually increased, focusing on the region of stress concentration "above" a hole as indicated by the dashed box in **Figure 3a**. For the centered square patterned surface with aspect ratio of D =80 μm, Φ = 40 μm, h =43 μm, we found the onset of wrinkling starts at a small compressive strain of ε = 0.02 (**Figure 3b-3c**) and progress to cover the region by ε = 0.11. The initial wavelength (λ_o) is predicted to be $\lambda_0 = (2\pi h_f)(\bar{E}_f/3\bar{E}_s)^{1/3}$, or 700 nm for an oxidized layer thickness of h_f = 55 nm, which is in reasonable agreement with the measured value of ~ 850 nm. The progressive wrinkling over this range of strain presumably reflects the influence of the energy boundaries resulting from the local curvature. We also find the creases start to nucleate at ε = 0.11, and start to grow at ε = 0.15, then fully cover the region at ε = 0.25. A hierarchical surface is formed at ε = 0.55, where we can see the periodic surface under the reflective optical microscopy in **Figure 3d**.

There is clearly a curvature guided formation of wrinkle at ε = 0.02 with non-uniform amplitude distribution which reveals the state of energy concentration, where the hole edge perpendicular to the compression axis scores the highest (**Figure 3c**). The period doubling pattern can be observed at ε = 0.15, with every second wrinkle growing in amplitude while its neighbors shrink. The strain value for this bifurcation is also smaller than the reported strain value ~ 0.17[5]. From ε = 0.15, further compression does not noticeably influence the in-plane morphology, since the AFM result cannot reflect the out of plane deformation towards the substrate, *i.e.* self-contact area of the crease. Therefore, we add the cross-sectional scanning data of the film from laser-scanning confocal fluorescence microscopy (LSCM, **Figure 3e**) to reveal the out of plane morphological development for the selected area (**Figure 3f**). At a strain of ε = 0.15 (**Figure 3c**), the LCSM data shows a shallow crease depth (self-contact area) within 100 nm, where it is considered as the onset of the crease.

Similar with the wrinkling, this second bifurcation is found to be highly sensitive to the presence of local planar curvature (**Figure S5**). At higher compressive strains, the crease depth develops under higher compressive strains and extends to all scanned areas.

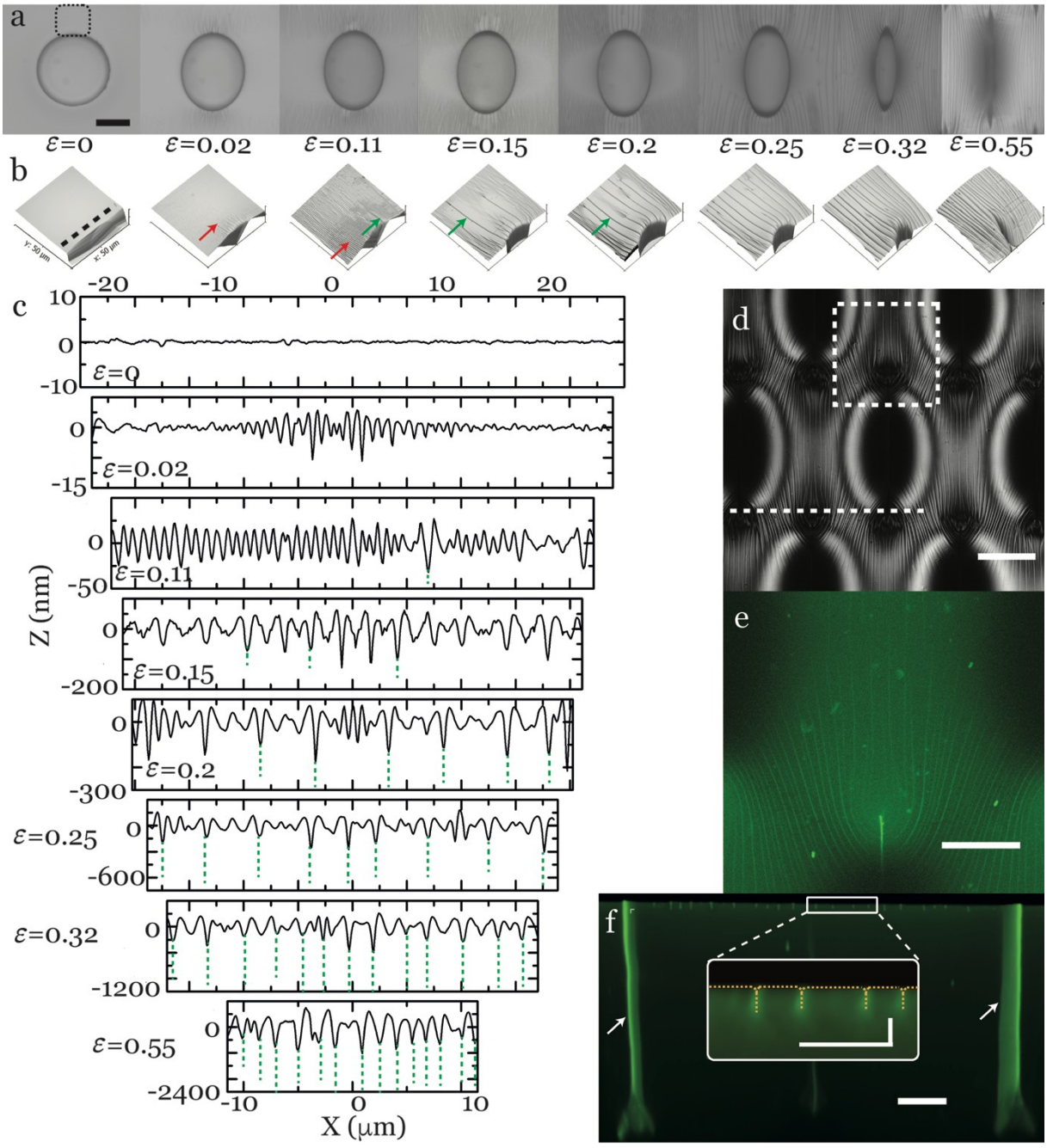

Figure 3. Characterization of the instabilities on the single hole and their evolutions under the uniaxial compression. (a) Top view observations and (b) AFM profiling of the selected area in (a) for surface morphology changes under the uniaxial compression for a unit area (centered square lattice array) with in-plane aspect ratio of D = 80 μm, Φ = 40 μm, h = 43 μm. (c) The surface morphology development is plotted with the

dependency on compression strain, the surface starts to initialize localized wrinkles on ε = 0.02, then develops into periodic doubling at ε = 0.15, the surface starts to form creases locally at ε = 0.2, where the sharp self-contacts within the PDMS (green dash lines) are detected by LCSM, and finally the creasing develops globally. (d) The reflective image shows a surface hierarchy formed when the hole reached the 'off' state at a compression deformation of 0.55. Laser confocal scanning reveals (e) the in-plane distribution of creases and (f) the out of plane morphology developed into the PDMS substrate for the selected area in (d), the arrows show the high intensity fluorescence signal due to the closure of neighbouring holes. The scale bar for the inset figure in (f) is 3 μm. The other scale bars are 40 μm.

We next consider the lattice pattern effects on post wrinkling bifurcations occurring at a higher strain level. It should be noted that the crease nucleates but it does not grow across the regime adjoining the lattice holes (**Figure S6**) for $D/\Phi \leq 1$. We expect this may arise due to the viscoelastic nature of the substrate, and/or the influence of large curvature. A brief classification of the transitions based on the crease number initiated is summarized in **Figure 4a-4c** for the lattice patterned surface with aspect ratio $D/\Phi > 1$. There are two transition types (single crease and multiple creases) for the stripe pattern, and the formation of creasing is revealed in **Figure 4d.** The 'star' type wrinkle pattern seems more likely to generate a single crease when being further compressed.

We next plot the normalized wrinkle amplitude (A/λ_0) as a function of the nominal applied strain on a non-patterned surface (**Figure 4e**) and a Bravais lattice patterned surface (**Figure 4f,** D = 80 μm, Φ = 40 μm, h = 43 μm). In each case, beyond wrinkling onset, two additional instabilities/bifurcations are seen, corresponding to period doubling and then crease formation. However, both the onset of wrinkling and the further bifurcations occur at considerably lower global strains in the patterned system: the critical wrinkle strain for the patterned surface of ~ 0.02 is less than one third of that in the flat surface (ε ~ 0.068), the critical strain for periodic doubling in the patterned surface is ~ 0.06, whereas it is ~ 0.18 in flat surface, and for the final bifurcation, the wrinkle-crease transition, the critical strain needed is ~ 0.08 in the patterned surface, which is less than half of that for the flat surface (ε

~ 0.22). We can understand this threshold reduction effect by considering the stress concentration in our analytic calculations for systems with $D/\Phi = 2$, (seen in **Figure 2g**), which exhibit a two-fold stress concentration at the edge of the hole relative to the non-patterned system, and hence predicts two-fold reduction in the various thresholds. The discrepancy between this calculation and the observed three-fold reduction is probably due to our analytic plane-strain approximation not capturing the full 3-D structure of the actual deformation field.

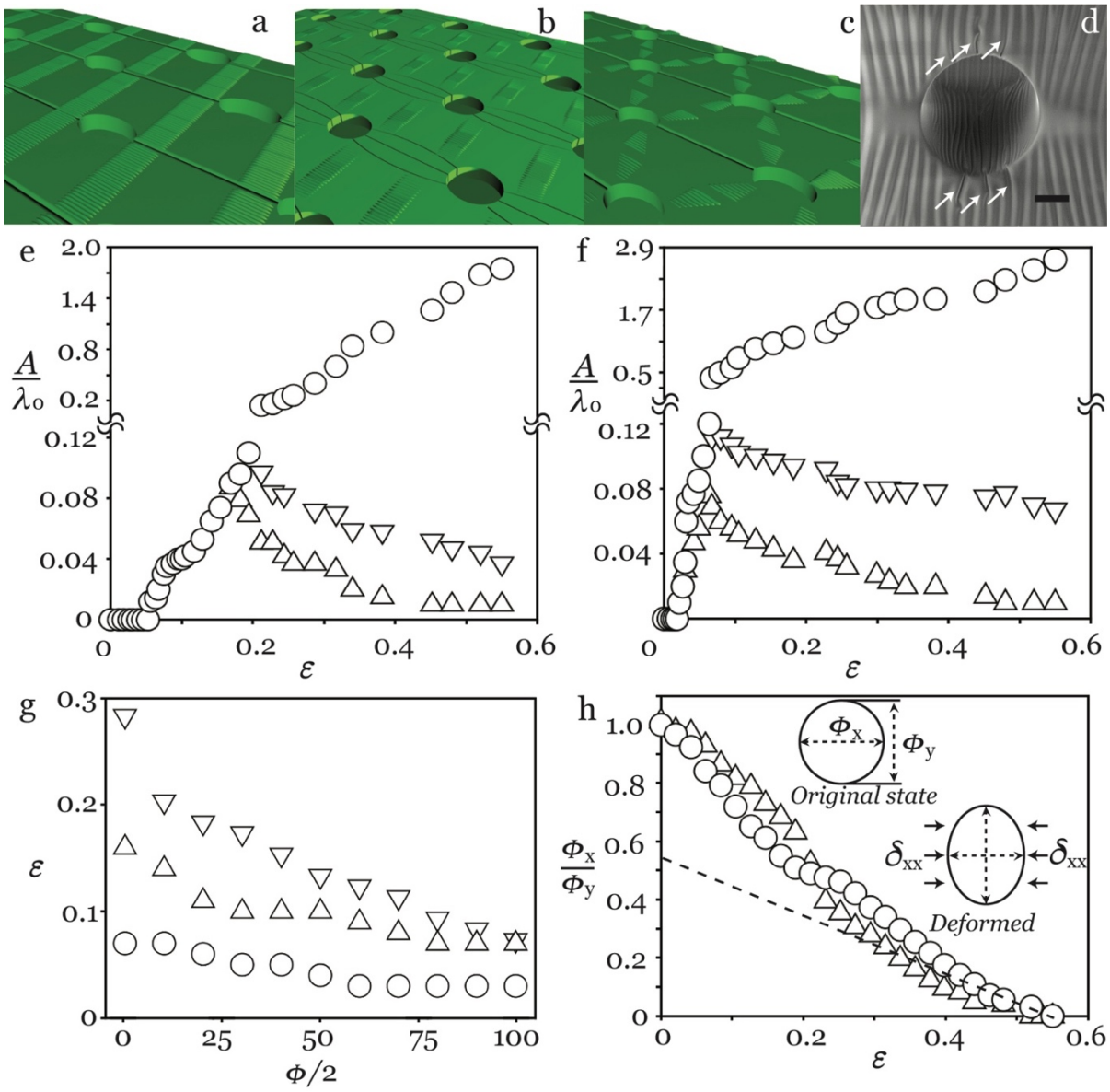

Figure 4. The evolution of surface morphology at higher compression, from wrinkling to creasing. Schematic illustrations of the transition from wrinkling to creasing for different harmonic patterns, (a) straight belt, (b) star shape, (c) curved ribbon. (d) SEM

image reveals the transition moment from wrinkling to creasing with the captured initialization of creases. The normalized amplitudes of surface features A/λ_0 reveal two post-wrinkling bifurcations with increasing strain for (e) homogeneous PDMS surface and (f) patterned PDMS surface (centered lattice) with in-plane aspect ratio of D = 80 μm, Φ = 40 μm, h = 43 μm. Normalised amplitudes changes along with two bifurcations and represented with first order (○), second order (△), and third order (▽). (g) The critical strains for initiating wrinkle (○), periodic doubling (△), creasing (▽) for the centered square array with different diameter. (h) The compression (△) and recovery (○) curves show the hysteresis and non-linearity on the deformation of a single hole under uniaxial compression.

It is important to understand quantitatively how these instabilities develop in the presence of the curved boundary from the edge of lattice holes. Thus, we plot the normalized strains for the onset of each instability as a function of the radius of lattice hole for D/Φ = 2. As seen in **Figure 4g**, the critical strains are clearly separated in different ranges, while the planar curvature decided by the radius of the holes influence the strains significantly. The overall strains are reduced as a result of the strain localization guided by the curved boundary, and it seems the strains for each instability are likely to collapse, which agrees well with the reported value by Kim that the doubling bifurcations are likely to be mixed with creasing with the $\bar{E}_f/\bar{E}_s$ value in the range of 14–47.[34,35] A key advantage of the elastic instability enabled technology is that, as an elastic process, it should yield a low degree of hysteresis. We then investigate the hysteresis of the lattice patterned surface with labelling the lateral dimension change in the hole (**Figure 4f**). The results suggest a robust transformation, which indicates that the viscoelastic relaxation of the soft PDMS layer used here is less important.

CONCLUSION

In this report, we present an approach to generate periodic planar wrinkle 2D patterns and controllable instability evolution towards a hierarchical surface by pre-placing Bravais lattice patterns on the surface as in-plane structural confinements. The bilayer system shows kinetic bistabilities at certain well-defined strain values initializing the

wrinkles and further elastic bifurcations at the designated areas/locations which are closely related to the geometries of the confinements. The formation of lateral wrinkle patterns has been studied with the dependencies on the geometrical variables of in-plane confinements and the results are in good agreement with the predictions from numerical analysis. At higher compression, we also reveal a targeted formation of wrinkle-to-crease transition as result of the reorganization of surface strain field. We anticipate this localized formation of surface instabilities, and the demonstration of bistability over a substantial range of strains will open new opportunities for applications of elastic instabilities on responsive surfaces for future lab on chip devices, by enabling delicate responses to mechanical inputs as selectively sensing or actuating structures.

METHOD

Micro-engineering and surface treatment of pattern template: Structural patterned templates of SU-8 micro-cylinders on silicon wafer were obtained through a standard photo-lithographic fabrication technique. Templates with different lattice arrays (square and centered square) and varied aspect ratios were prepared. A SAM of Trichloro(1H,1H,2H,2H-perfluorooctyl)silane (Sigma-Aldrich), was applied from the vapour phase at 20 °C for 30 min to facilitate subsequent release of the PDMS film.

Fabrication of Structural Confined Elastic Bilayer: The mounting layer was made from a commercial available elastomer product (Elite Double 22, shear modulus ~ 0.35 MPa) from Zhermack Ltd. After mixing the vinylpolysiloxane base with a curing agent with a weight ratio of 1:1 for 1 minute, the mixture was cured in the petri dish at 20 °C for 6 hours. The cured elastomeric film was ~ 3 mm in thickness, and a stripe of ~ 6 × 20 mm was cut and pre-stretched to 400% of its original length on a uniaxial mechanical strain stage. The soft PDMS layer with thickness of 125 μm (Sylgard 184, Dow Corning, 30:1 for elastomer base:crosslinker) was prepared by spin-coating the degassed mixture on a SU-8 patterned

silicon wafer (~1 cm^2) at 1000 rpm for 120 s, followed by curing at 70 °C for 1 h. An adhesive PDMS layer with the same composition of 30:1 was spin-coated on this cured layer at 3000 rpm for 120 s, to bond to the mounting layer. After transferring the adhesive coated soft PDMS layer to the mounting layer, the assembly was baked at 70 °C for 8 h to cure the adhesive layer. Prior to characterization, the bilayer was treated with oxygen plasma (HPT-100, Henniker) under a working power of 100 watt, with a mixed gas atmosphere of oxygen/nitrogen ratio ~ 0.2.

Characterization: The bilayer was progressed to measurement as soon as the oxygen plasma treatment was completed. Incremental deformation in nominal strain of ~ 0.004 were applied to the sample by releasing the mounting layer pre-stretch by a fixed amount at regular intervals and situated for 15 min in room temperature. Sample surfaces were observed in situ using an upright optical microscope (Nikon LV-100) in brightfield reflection mode. For the laser scanning confocal microscopic imaging (Nikon A1R), the top layer was labelled by adding a small amount of fluorescent monomer (0.1 mg fluorescein-o-acrylate per 1 g PDMS). Scanning electron microscopy (MIRA3, TESCAN) was used to observe the surface structure. The surface topographic features were assessed with an atom force microscopy (D3100, Veeco).

Numerical analysis: Our numerical analysis used a finite element package in Mathematica to solve the 2D plain-strain linear elasticity problem for the deformation in the patterned soft substrate. We first defined a repeatable 2D unit cell with the geometry corresponding to the experiment and, as seen in Figure S7, described the domain by a fine mesh consisting of around 4000 triangles.

We then assumed a plain-strain deformation, described by the 2D displacement field $(u(x,y)\,\hat{\boldsymbol{x}} + v(x,y)\,\hat{\boldsymbol{y}})$ so the plain-strain stress tensor is

$$\sigma = \frac{E}{(1+\nu)}\begin{pmatrix} \frac{(1-\nu)u_{,x} + \nu v_{,y}}{(1-2\nu)} & \frac{u_{,y} + v_{,x}}{2} \\ \frac{u_{,y} + v_{,x}}{2} & \frac{\nu u_{,x} + (1-\nu)v_{,y}}{(1-2\nu)} \end{pmatrix},$$

where E is the Young's modulus, ν is the Poisson's ratio, and the comma-notation denotes partial derivatives. We then used the Mathematica finite element package to solve $\nabla \cdot \sigma = \mathbf{0}$ in the meshed domain, subject to the boundary conditions that $\sigma.\hat{\boldsymbol{n}} = \mathbf{0}$ on the hole edges, and that the straight edges of the cell move with the macroscopic strain of the underlying substrate (-ε in the x-direction and 0.3ε in the y-direction) as seen in Figure S7.

After solving for the displacement fields (Figure 2e), the stress on the film can be evaluated from the stress tensor above. To determine whether the region is unstable towards wrinkling, we diagonalized the stress tensor to find its maximum compressive stress (Figure 2g). By comparing this compressive stress with the theoretical critical value, we can identify the wrinkling region (Figure 2f), while the wrinkle direction (the short lines in Figure 2f) was perpendicular to the principal direction of the maximum compressive stress.

Acknowledgements

The work was supported by the Engineering and Physical Sciences Research Council (EPSRC) grant-EP/N007921/1 and Royal Society research grant-RG150662. Dr Ben Bin Xu and Mr Ding Wang would thank Reece Innovation for the studentship support and Dr. Gary Wells for the useful discussions.

Received: ((will be filled in by the editorial staff))
Revised: ((will be filled in by the editorial staff))
Published online: ((will be filled in by the editorial staff))

References

[1] N. Bowden, S. Brittain, A. G. Evans, J. W. Hutchinson, G. M. Whitesides, *Nature* **1998**, *393*, 146.
[2] D. Chen, J. Yoon, D. Chandra, A. J. Crosby, R. C. Hayward, *J. Polym. Sci. Part B Polym. Phys.* **2014**, *52*, 1441.
[3] P. Kim, M. Abkarian, H. A. Stone, *Nat. Mater.* **2011**, *10*, 952.
[4] E. Hohlfeld, L. Mahadevan, *Phys. Rev. Lett.* **2011**, *106*, 105702.
[5] F. Brau, H. Vandeparre, A. Sabbah, C. Poulard, A. Boudaoud, P. Damman, *Nat. Phys.* **2011**, *7*, 56.
[6] T. Tallinen, J. Y. Chung, J. S. Biggins, L. Mahadevan, *Proceedings of the National Academy of Sciences* **2014**, *111*, 12667.
[7] D. Chen, S. Cai, Z. Suo, R. C. Hayward, *Phys. Rev. Lett.* **2012**, *109,* 038001.
[8] B. Xu, R. C. Hayward, *Adv. Mater.* **2013**, *25*, 5555.
[9] J. Kim, J. A. Hanna, M. Byun, C. D. Santangelo, R. C. Hayward, *Science*, **2012**, *335*, 1201.
[10] S.-J. Jeon, A. W. Hauser, R. C. Hayward, *Accounts. Chem. Res.* **2017**, *50*, 161.
[11] Y. Liu, J. K. Boyles, J. Genzer, M. D. Dickey, *Soft Matter* **2012**, *8*, 1764.
[12] M. A. C. Stuart, W. T. S. Huck, J. Genzer, M. Muller, C. Ober, M. Stamm, G. B. Sukhorukov, I. Szleifer, V. V. Tsukruk, M. Urban, F. Winnik, S. Zauscher, I. Luzinov, S. Minko, *Nat. Mater.* **2010**, *9*, 101.
[13] B. B. Xu, Q. Liu, Z. Suo, R. C. Hayward, *Adv. Funct. Mater.* **2016**, *26*, 3218.
[14] D. P. Holmes, B. Tavakol, G. Froehlicher, H. A. Stone, *Soft Matter* **2013**, *9*, 7049.
[15] T. Ohzono, H. Monobe, *Langmuir* **2010**, *26*, 6127.
[16] S.-m. Park, Y. S. Huh, H. G. Craighead, D. Erickson, *Proceedings of the National Academy of Sciences* **2009**, *106*, 15549.
[17] B. Xu, D. Chen, R. C. Hayward, *Adv. Mater.* **2014**, *26*, 4381.
[18] J. A. Rogers, T. Someya, Y. Huang, *Science* **2010**, *327*, 1603.
[19] P.-C. Lin, S. Vajpayee, A. Jagota, C.-Y. Hui, S. Yang, *Soft Matter* **2008**, *4*, 1830.
[20] E. P. Chan, E. J. Smith, R. C. Hayward, A. J. Crosby, *Adv. Mater.* **2008**, *20*, 711.
[21] J. B. Kim, P. Kim, N. C. Pegard, S. J. Oh, C. R. Kagan, J. W. Fleischer, H. A. Stone, Y. L. Loo, *Nat. Photonics* **2012**, *6*, 327.
[22] P. Görrn, M. Lehnhardt, W. Kowalsky, T. Riedl, S. Wagner, *Adv. Mater.* **2011**, *23*, 869.
[23] E. Lee, M. Zhang, Y. Cho, Y. Cui, J. Van der Spiegel, N. Engheta, S. Yang, *Adv. Mater.* **2014**, *26*, 4127.
[24] S.S. Zeng, D.Y. Zhang, W.H. Huang, Z.F. Wang, S.G. Freire, X.Y. Yu, A.T. Smith, E. Y. Huang, H. Nguon, L. Sun, *Nat. Commun.* **2016**, *7*, 11802.
[25] K. Khare, J. Zhou, S. Yang, *Langmuir* **2009**, *25*, 12794.
[26] S. G. Lee, D. Y. Lee, H. S. Lim, D. H. Lee, S. Lee, K. Cho, *Adv. Mater.* **2010**, *22*, 5013.
[27] X. Huang, Y. Sun, S. Soh, *Adv. Mater.* **2015**, *27*, 4062.
[28] J. Kim, J. Yoon, R. C. Hayward, *Nat. Mater.* **2010**, *9*, 159.
[29] M. Arifuzzaman, Z. L. Wu, R. Takahashi, T. Kurokawa, T. Nakajima, J. P. Gong, *Macromolecules* **2013**, *46*, 9083.
[30] Q. Li, X. Han, J. Hou, J. Yin, S. Jiang, C. Lu, *The Journal of Physical Chemistry B* **2015**, *119*, 13450.
[31] J. Rodríguez-Hernández, *Prog. Polym. Sci.* **2015**, *42*, 1.
[32] A. Auguste, L. Jin, Z. Suo, R. C. Hayward, *Extreme Mechanics Letters* **2017**, *11*, 30.
[33] T. Tallinen, J. S. Biggins, *Phys. Rev. E* **2015**, *92*, 022720.

[34] M. Diab, T. Zhang, R. Zhao, H. Gao, K.-S. Kim, *Proceedings of the Royal Society A: Mathematical, Physical and Engineering Science* **2013**, *469,*20120753.
[35] R. Zhao, T. Zhang, M. Diab, H. Gao, K.-S. Kim, *Extreme Mechanics Letters* **2015**, *4*, 76.
[36] W.T. S. Huck, N. Bowden, P. Onck, T. Pardoen, J.W. Hutchinson, G. M. Whitesides, *Langmuir* **2000**, *16*, 3497.
[37] Q. Wang, X. Zhao, *Scientific Reports* **2015**, *5*, 8887.
[38] Q. Wang, X. Zhao, *Mrs. Bull.* **2016**, *41*, 115.
[39] D. Breid, A. J. Crosby, *Soft Matter* **2013**, *9*, 3624.
[40] N. Stoop, R. Lagrange, D. Terwagne, P. M. Reis, J. Dunkel, *Nat. Mater.* **2015**, *14*, 337.
[41] J. D. Paulsen, E. Hohlfeld, H. King, J. Huang, Z. Qiu, T. P. Russell, N. Menon, D. Vella, B. Davidovitch, *Proceedings of the National Academy of Sciences* **2016**, *113*, 1144.
[42] F. L. Jim´enez, N. Stoop, R. Lagrange, J. Dunkel and P. M. Reis, *Phys. Rev. Lett.* **2016**, *116*,104301.
[43] Y. Cao, J. W. Hutchinson, *J. Appl. Mech.* **2012**, *79*, 031019.
[44] H. G. Allen, in *Analysis and Design of Structural Sandwich Panels*, Pergamon, 1969.
[45] J. Genzer, J. Groenewold, *Soft Matter* **2006**, *2*, 310.
[46] R. W. Bailey, R. Fidler, *Nucl. Eng. Des.* **1966**, *3*, 41.
[47] M. L. Kachanov, B. Shafiro, I. Tsukrov, *Handbook of Elasticity Solutions*, Springer Netherlands, 2003.
[48] H. Jiang, D.-Y. Khang, J. Song, Y. Sun, Y. Huang, J. A. Rogers, *Proceedings of the National Academy of Sciences* **2007**, *104*, 15607.

The table of contents

Taking advantage of patterning lattice holes on an elastic bilayer, we demonstrate the formation of versatile wrinkle patterns that selectively cover the substrate and provide controllable evolution of the instability morphology to achieve a hierarchical surface. This provides insight into the formation and evolution of elastic instabilities on complex surfaces.

Keyword: Elastic instabilities, Wrinkling, Micro-pattern, Bravais lattice, Morphological bifurcation.

By Ding Wang,[1] Nontawit Cheewaruangroj,[2] Yifan Li, [1] Glen McHale,[1] Yinzhu Jiang,[3] David Wood,[4] John Simeon Biggins,[2]* Ben Bin Xu[1]*

Title: Spatially configuring wrinkle pattern and multi-scale surface evolution with structural confinement

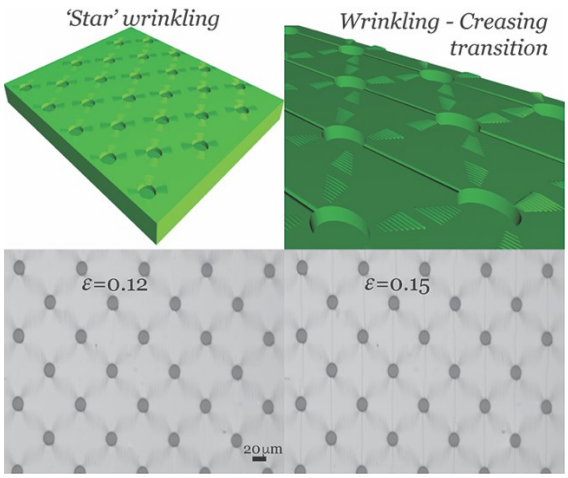

Supporting Information

Title: Spatially configuring wrinkle pattern and multi-scale surface evolution with structural confinement

By *Ding Wang,[1] Nontawit Cheewaruangroj,[2] Yifan Li,[1] Glen McHale,[1] Yinzhu Jiang,[3] David Wood,[4] John Simeon Biggins,[2]* Ben Bin Xu[1]**

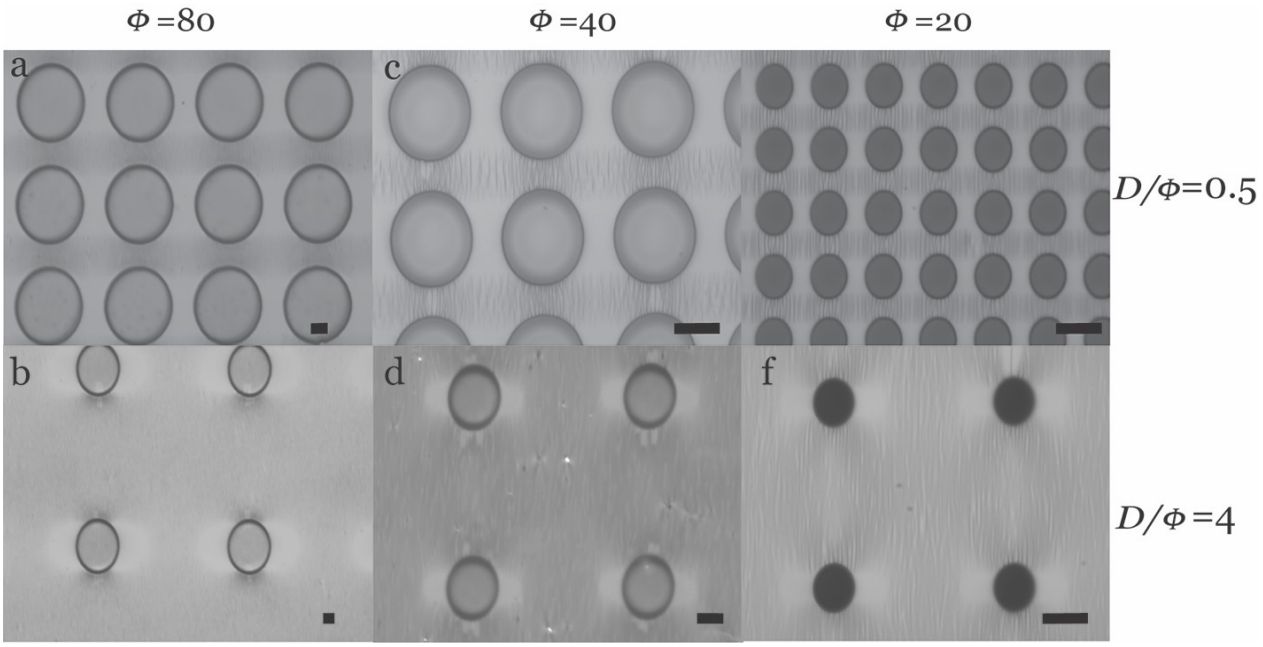

Figure S1. The formation of the lateral wrinkle pattern for the square lattice patterned surface with different geometrical aspect ratio.

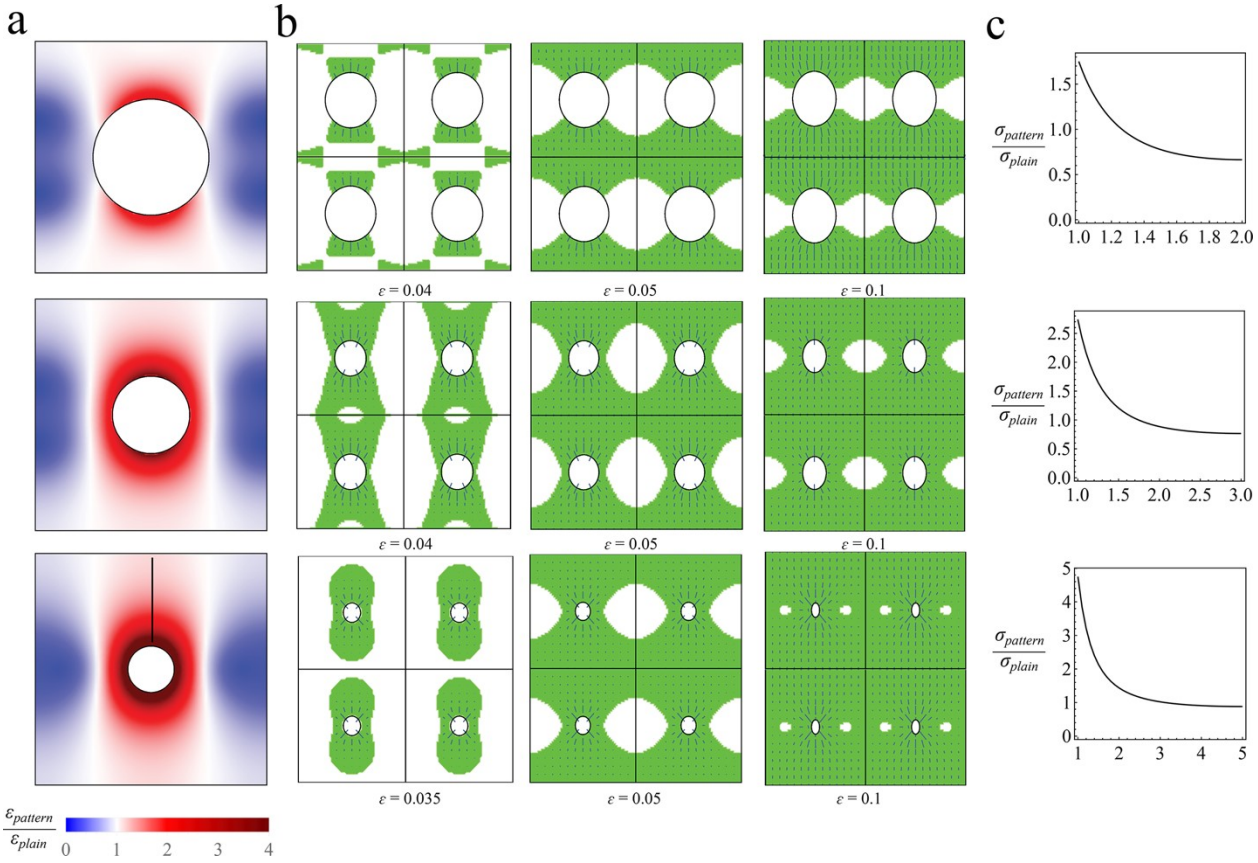

Figure S2. Numerical simulation of the wrinkle pattern generation on square lattice patterned surfaces. (a) Compression of the patterned substrate relative to the compression of the non-patterned substrate. Blue and red indicate the less and more compressive areas. (b) Evolution of wrinkling region as a function of a bilayer system with patterned holes. Green areas are the wrinkling regions. Lines indicate the direction along which the wrinkles will grow while their lengths are the relative distance from the wrinkling threshold. (c) Compressive stress in the stiff layer in the patterned bilayer system relative to the non-patterned system values at different position from the rim of the hole of radius a (maximum stress) to the edge of the unit cell (see arrow in (c) bottom). All plotted with D/Φ = 1, 2 and 4.

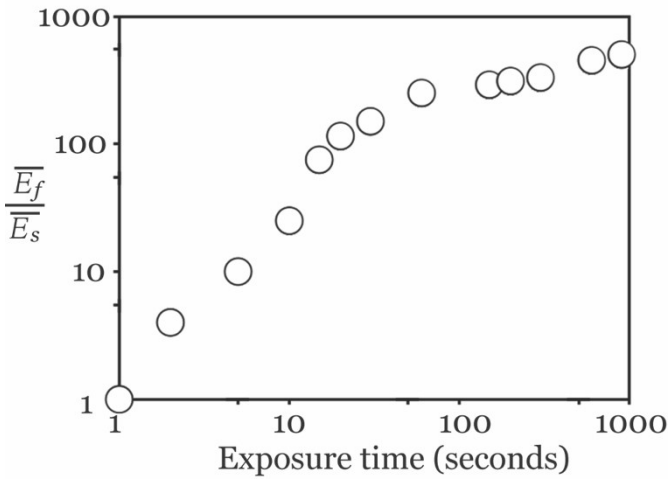

Figure S3. The modulus mismatch as a function of plasma treating duration.

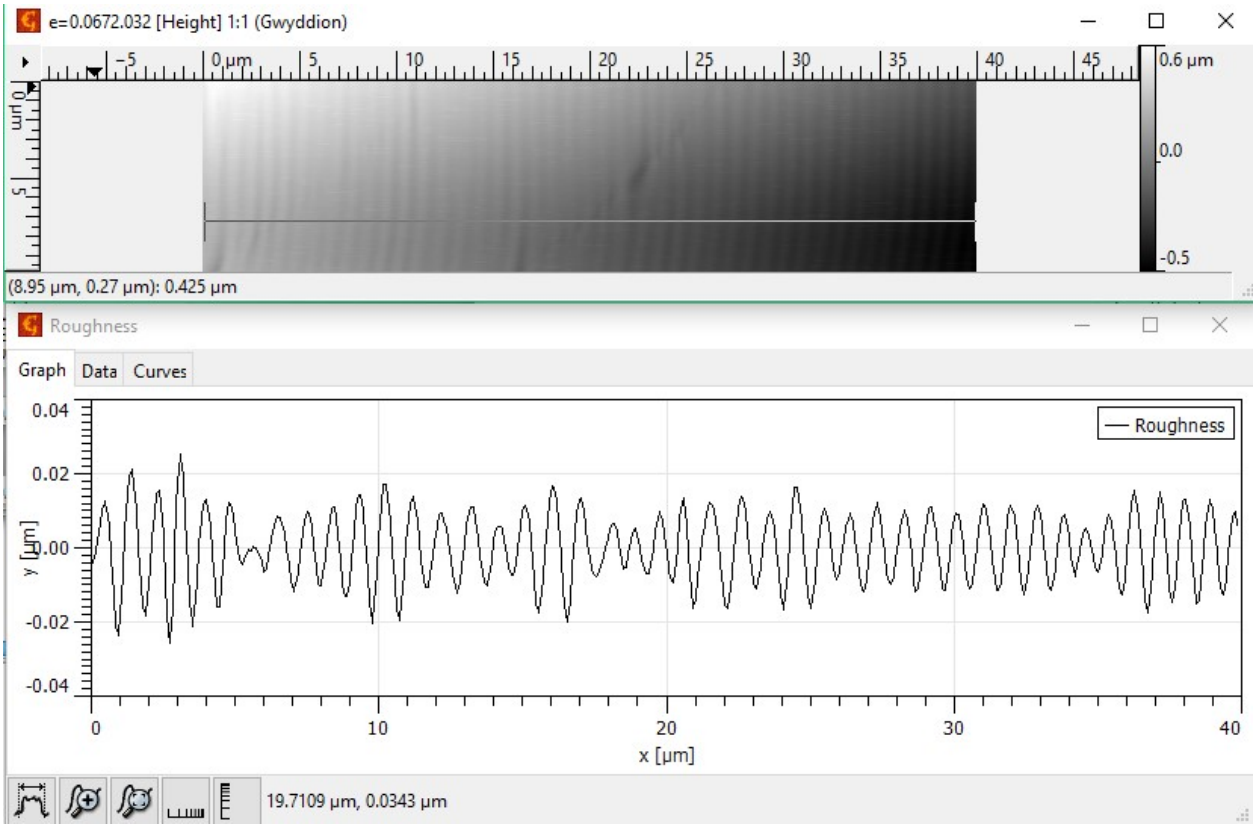

Figure S4. The onset of wrinkle at a critical strain of 0.0672 for non-patterned PDMS surface under plasma treatment for 10 seconds.

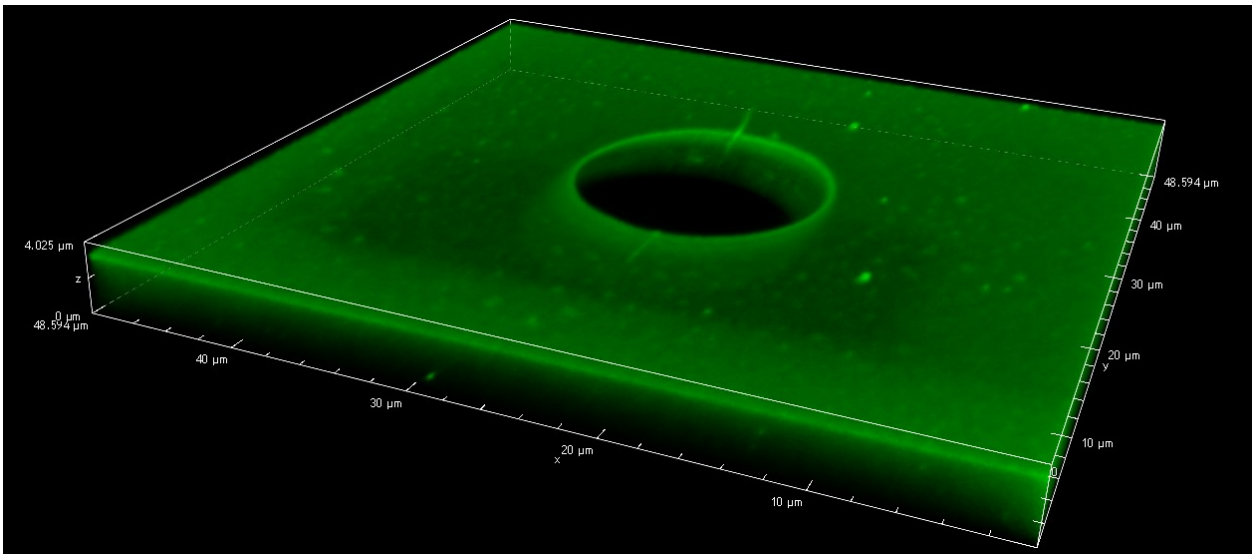

Figure S5. The LCSM scanning to view the initialising of the creasing on the targeted area for the centered square lattice patterned surface with aspect ratio of Φ=20µm, h=43µm, D/Φ =4.

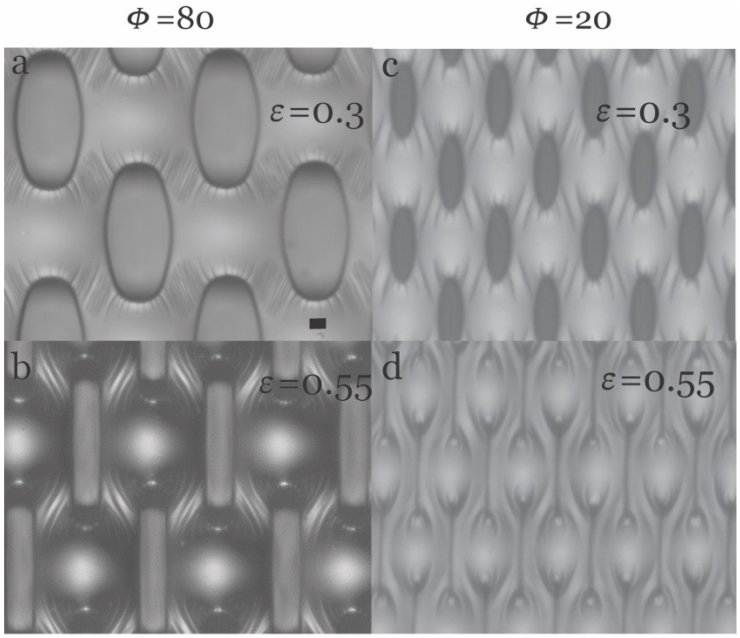

Figure S6. The deformation of patterned surface under higher compression with different hole diameter.

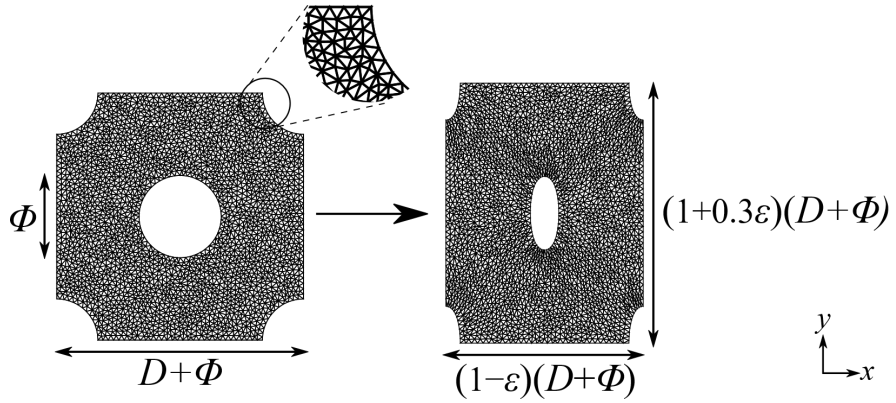

Figure S7. Discretized mesh elements for the numerical analysis of a unit cell: (left) non-deformed unit cell, (right) deformed unit cell with a macroscopic strain ε = 0.2.